Probing Non-Equilibrium Grain Boundary Dynamics with XPCS and Domain-Adaptive Machine Learning: Supplementary Information

Mouyang Cheng[1,2,3,†,*], Bowen Yu[1,4,†], Chu-Liang Fu[1,5], Nina Andrejevic[6], Matthias T. Agne[7], Riley Hanus[8], Qiwei Wan[1,5], Nathan C. Drucker[1,9], Thanh Nguyen[1,5], Andrei Fluerasu[10], Lutz Wiegart[10], Xiaoqian M Chen[10], Daniel Pajerowski[11], Yongqiang Cheng[11], Joshua J Turner[12], G. Jeffrey Snyder[8], and Mingda Li[1,2,5,]**

[1]Quantum Measurement Group, MIT, Cambridge, MA 02139, USA
[2]Center for Computational Science and Engineering, MIT, Cambridge, MA 02139, USA
[3]Department of Materials Science and Engineering, MIT, Cambridge, MA 02139, USA
[4]Department of Physics, MIT, Cambridge, MA 02139, USA
[5]Department of Nuclear Science and Engineering, MIT, Cambridge, MA 02139, USA
[6]Center for Nanoscale Materials, Argonne National Laboratory, Lemont, IL 60439, USA
[7]Materials Science Institute, University of Oregon, Eugene, OR 97403, USA
[8]Department of Materials Science and Engineering, Northwestern University, Evanston, IL 60208, USA
[9]Department of Applied Physics, School of Engineering and Applied Sciences, Harvard University, Cambridge, MA 02138, USA
[10]National Synchrotron Light Source II, Brookhaven National Laboratory, Upton, NY 11973, USA
[11]Neutron Scattering Division, Oak Ridge National Laboratory, Oak Ridge, TN 37831, USA
[12]SLAC National Accelerator Laboratory, Menlo Park, CA 94025, USA
[†]These authors contributed equally.
[*]e-mail: vipandyc@mit.edu
[**]e-mail: mingda@mit.edu

Contents

1 Observables from XPCS **2**

2 Experimental and simulated data for XPCS **2**

2.1 Experimental XPCS data . . . 2

2.2 Simulated XPCS data and the non-equilibrium phase landscape . . . 5

2.3 Diffusion from molecular dynamics simulation . . . 8

3 Additional results on domain-adaptive machine learning **8**

3.1 Effects of smearing and rescaling on experimental XPCS data . . . 9

3.2 Alternative machine-learning methods for domain alignment . . . 10

3.3 Ablation tests on hyperparameters . . . 11

3.4 Outlier experimental XPCS data on the simulated parameter manifold . . . 13

References **14**

1 Observables from XPCS

We review the XPCS observables used to connect the measured two-time correlation maps with density fluctuations in the material with the grain boundary (GB). We begin from the standard Siegert relation[1], which relates the measured two-time intensity correlation to the intermediate scattering function,

$$g_2(\mathbf{Q},t,t') = 1 + |g_1(\mathbf{Q},t,t')|^2 \tag{S1}$$

$$g_1(\mathbf{Q},t,t') = \frac{\langle \rho(-\mathbf{Q},t)\rho(\mathbf{Q},t')\rangle}{\langle \rho(-\mathbf{Q},t)\rho(\mathbf{Q},t)\rangle} \tag{S2}$$

where g_1 characterizes the density-density correlation, and we write the electron density operator as

$$\rho(\mathbf{Q},t) = \sum_{j=1}^{N} f_j(\mathbf{Q}) e^{-i\mathbf{Q}\cdot\mathbf{r}_j(t)}. \tag{S3}$$

We consider a system containing both bulk-like atoms and atoms associated with a grain-boundary environment, and introduce a time-dependent character function $\chi_j(t)$ to indicate whether atom j belongs to the grain-boundary environment at time t. With this decomposition, the density-density correlation can be separated into GB-associated and bulk-associated contributions,

$$\left\langle \rho(-\mathbf{Q},t)\rho(\mathbf{Q},t')\right\rangle = \left\langle \rho(-\mathbf{Q},t)\rho(\mathbf{Q},t')\right\rangle_{\mathrm{GB}} + \left\langle \rho(-\mathbf{Q},t)\rho(\mathbf{Q},t')\right\rangle_{\mathrm{bulk}}. \tag{S4}$$

For the bulk contribution, we treat the particles as identical scatterers undergoing Brownian motion, which gives the corresponding intermediate scattering function,

$$g_1(\mathbf{Q},t,t') = \frac{|f(\mathbf{Q})|^2}{N} \left\langle \sum_{ij}^{N} e^{i\mathbf{Q}\cdot(\mathbf{r}_i(t)-\mathbf{r}_j(t))} \right\rangle. \tag{S5}$$

When the particle displacements are Gaussian random variables, we obtain

$$g_1(\mathbf{Q},t,t') = \frac{|f(\mathbf{Q})|^2}{N} \sum_{j=1}^{N} \exp\left(-\frac{1}{6} \sum_{a=1,2,3} \mathbf{Q}_a^2 2D_0 t \right) = |f(\mathbf{Q})|^2 e^{-\mathbf{Q}^2 D_0 t}. \tag{S6}$$

Thus, combining the simulation protocol described in the main text, one can perform batch simulation on $g_2(\mathbf{Q},t,t')$ under different effective parameters characterizing the nanocrystalline silicon.

2 Experimental and simulated data for XPCS

In this section, we present additional experimental measurements for XPCS data, as well as simulated XPCS mapping from the continuum model.

2.1 Experimental XPCS data

Additional experimental XPCS maps and non-equilibrium characterization are shown for four sample groups not included in Fig. 2 in the main text, as shown in Fig. S1 to Fig. S4. These measurements include a 0.72% GaP sample (Fig. S1), a 96.4% Si lump, 2.16% P, and 0.72% GaP sample milled for 24 h (Fig. S2), a 99.0% Si and 1.0% P sample milled for 24 h (Fig. S3), and an undoped Si (Fig. S4).

The four supplementary groups show distinct detailed GB dynamics, while all of them exhibit a transition from equilibrium to non-equilibrium as temperature rises. The P/GaP-doped Si sample already develops a strong non-equilibrium response by 416 K, with $\mathscr{S}_{\mathrm{noneq}}$ increasing from 0.213 at 298 K to 0.725 at 416 K, and the high-temperature map retains pronounced block-like structure at 467 K. The 24 h milled P/GaP-doped sample shows an even earlier onset, reaching $\mathscr{S}_{\mathrm{noneq}} = 0.721$ at 371 K and remaining strongly non-equilibrium at 450 K, and the 24 h milled P-doped sample evolves more gradually from $\mathscr{S}_{\mathrm{noneq}} = 0.347$ at 299 K to 0.736 at 468 K. By comparison,

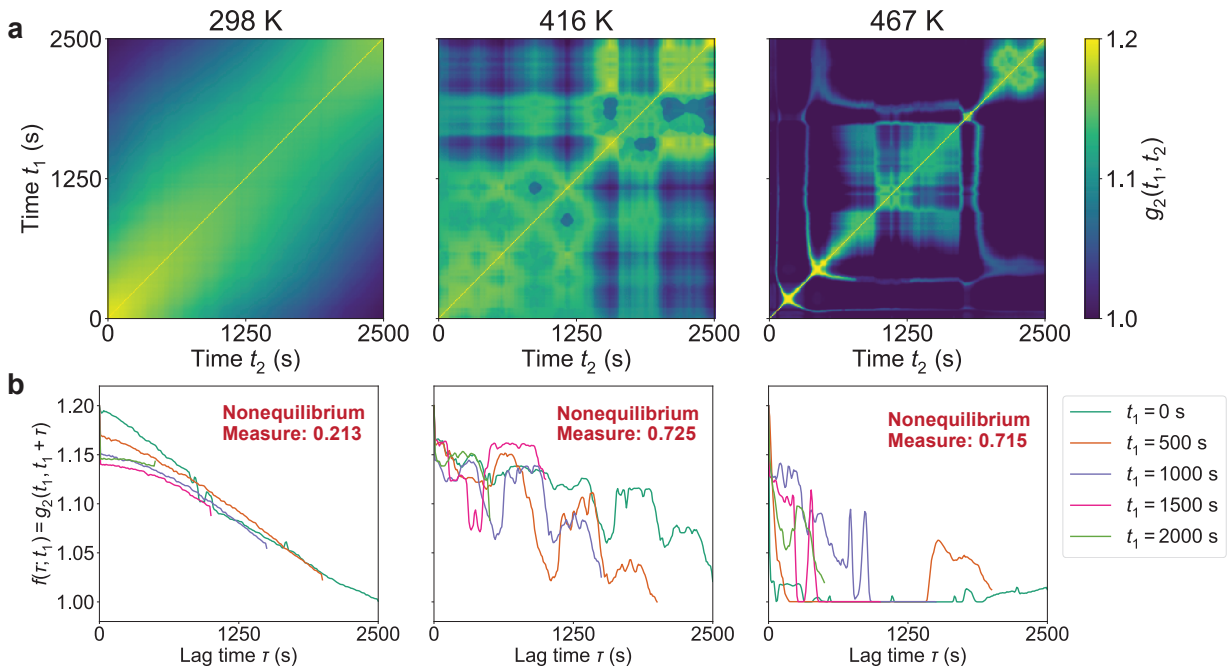


Figure S1. Experimental XPCS maps and intensity-intensity correlation slices for P/GaP-doped Si. Temperature-dependent two-time correlation maps and corresponding intensity-intensity correlation slices $f(\tau;t_1) = g_2(t_1, t_1 + \tau)$ at different times t_1 for the 96.4% Si, 2.16% P, and 0.72% GaP sample.

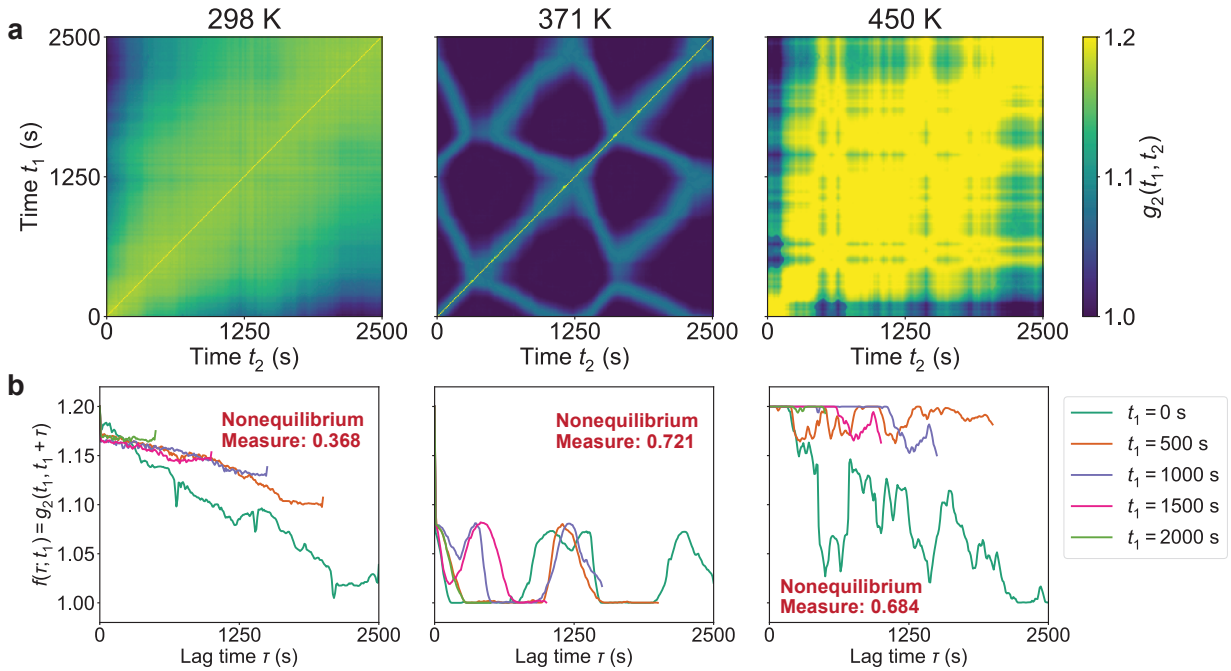


Figure S2. Experimental XPCS maps and intensity-intensity correlation slices for 24 h milled P/GaP-doped Si. Temperature-dependent two-time correlation maps and corresponding intensity-intensity correlation slices $f(\tau;t_1) = g_2(t_1, t_1 + \tau)$ at different times t_1 for the 96.4% Si, 2.16% P, and 0.72% GaP sample milled for 24 h.

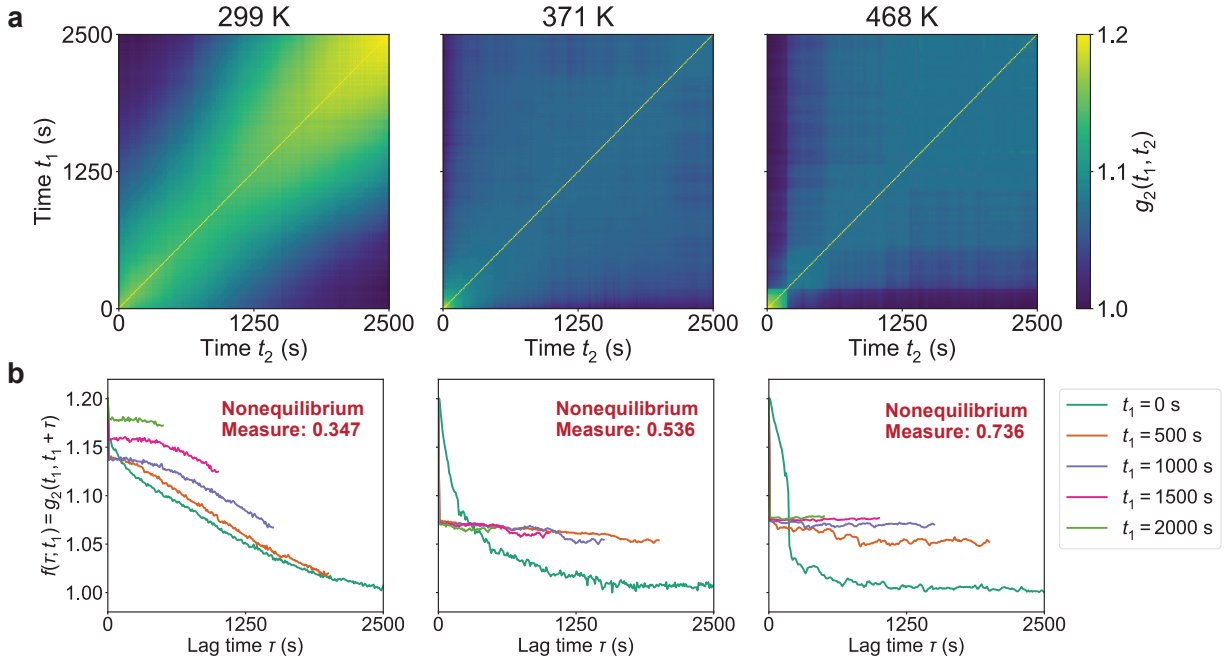


Figure S3. Experimental XPCS maps and intensity-intensity correlation slices for 24 h milled P-doped Si. Temperature-dependent two-time correlation maps and corresponding intensity-intensity correlation slices $f(\tau;t_1) = g_2(t_1, t_1+\tau)$ at different times t_1 for the 99.0% Si and 1.0% P sample milled for 24 h.

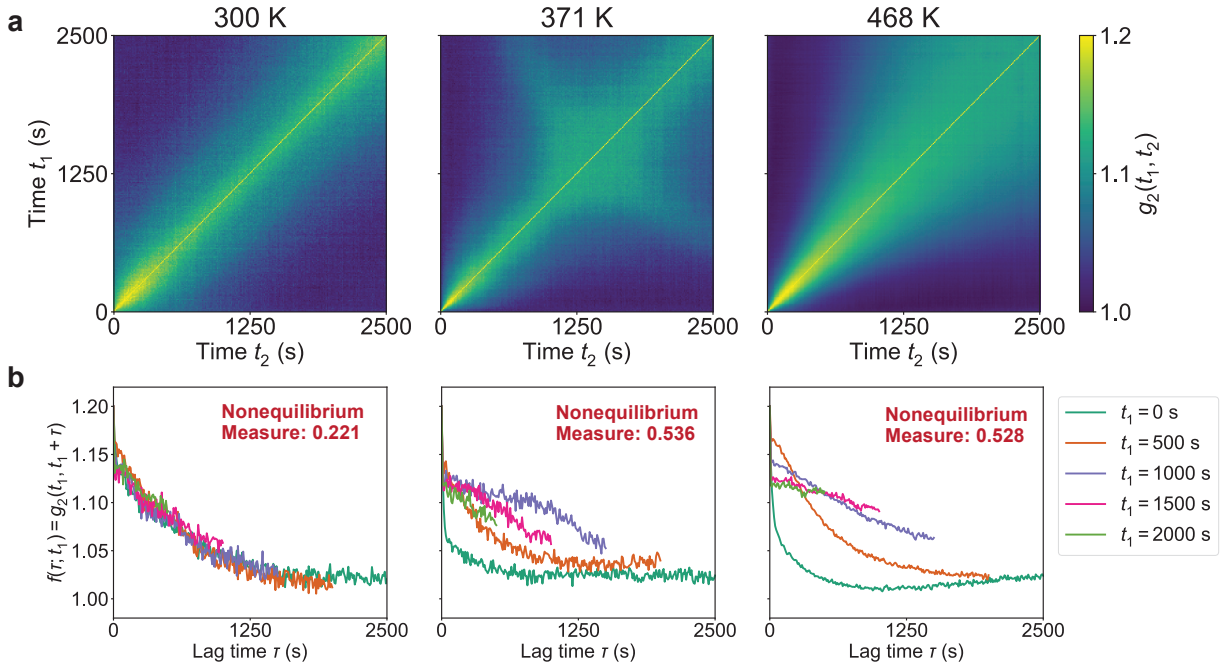


Figure S4. Experimental XPCS maps and intensity-intensity correlation slices for undoped Si. Temperature-dependent two-time correlation maps and corresponding intensity-intensity correlation slices $f(\tau;t_1) = g_2(t_1, t_1+\tau)$ at different times t_1 for undoped Si.

undoped Si shows a smoother broadening of the diagonal correlation ridge, with moderate non-equilibrium measures of 0.536 and 0.528 at 371 K and 468 K, respectively. These source maps therefore show that the non-equilibrium XPCS response is observed across the measured Si-based samples, while its onset temperature, spatial texture in $g_2(t_1,t_2)$, and separation of the intensity-intensity correlation slices depend strongly on dopant composition and milling history.

2.2 Simulated XPCS data and the non-equilibrium phase landscape

To complement the simulated XPCS maps in the $(D,\lambda_{\mathrm{GB}})$ parameter space shown in Fig. 3 in the main text, Figs. S5–S7 display fixed-λ_{GB} slices at low, intermediate, and high effective GB concentrations, revealing how the non-equilibrium response evolves as the bulk diffusivity D is varied according to our continuum model. Across these slices, the high-$\mathscr{S}_{\mathrm{noneq}}$ region follows an oblique crossover in the $(D,\lambda_{\mathrm{GB}})$ plane, with only the slowest bulk-diffusion cases remaining strongly non-equilibrium at low λ_{GB}.

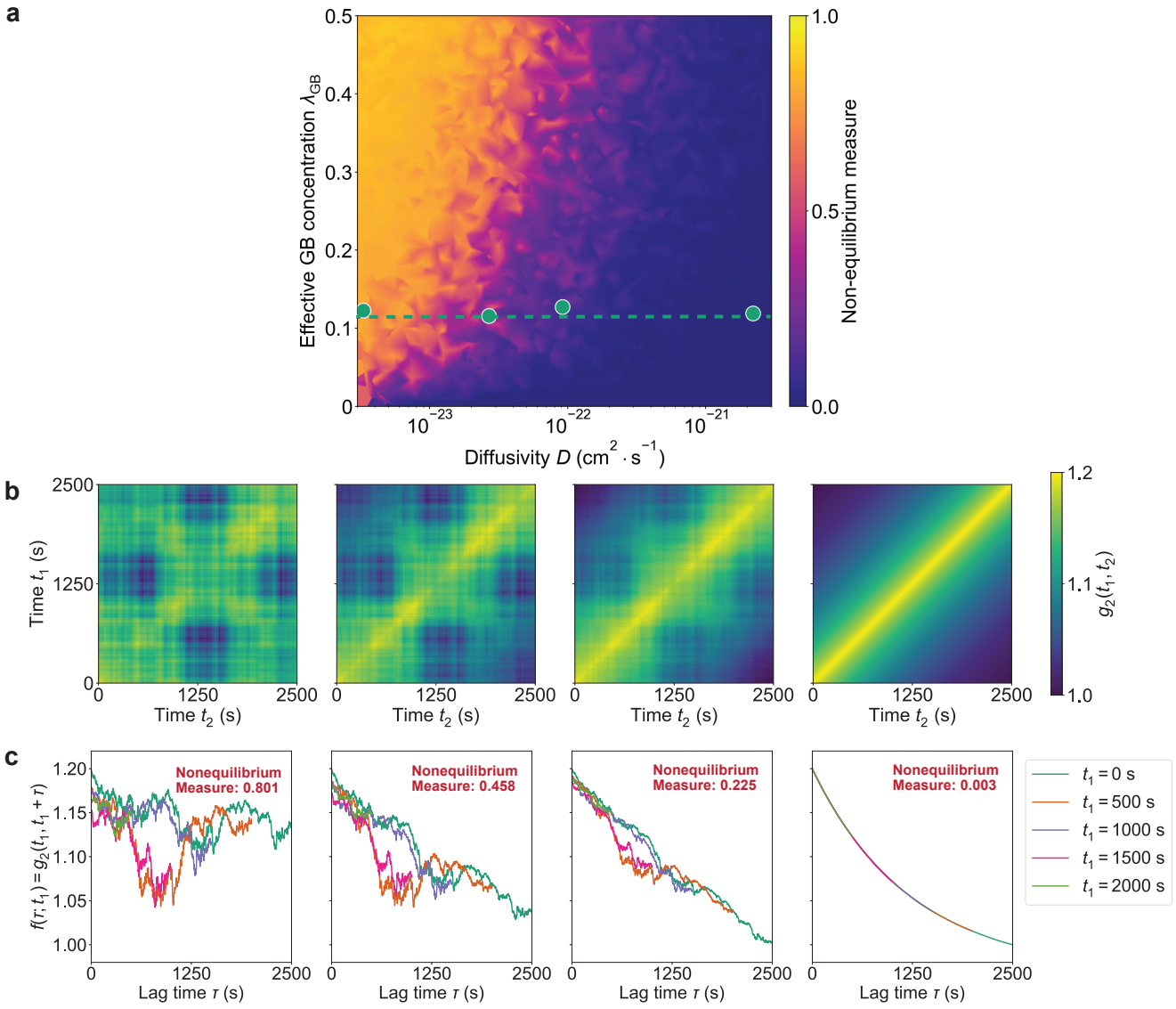


Figure S5. Simulated XPCS dynamics selected along increasing diffusivity at low effective GB concentration. Four simulations near $\lambda_{\mathrm{GB}} = 0.12$ are shown along increasing D, with the corresponding raw non-equilibrium scores decreasing from strongly non-stationary to nearly equilibrated dynamics.

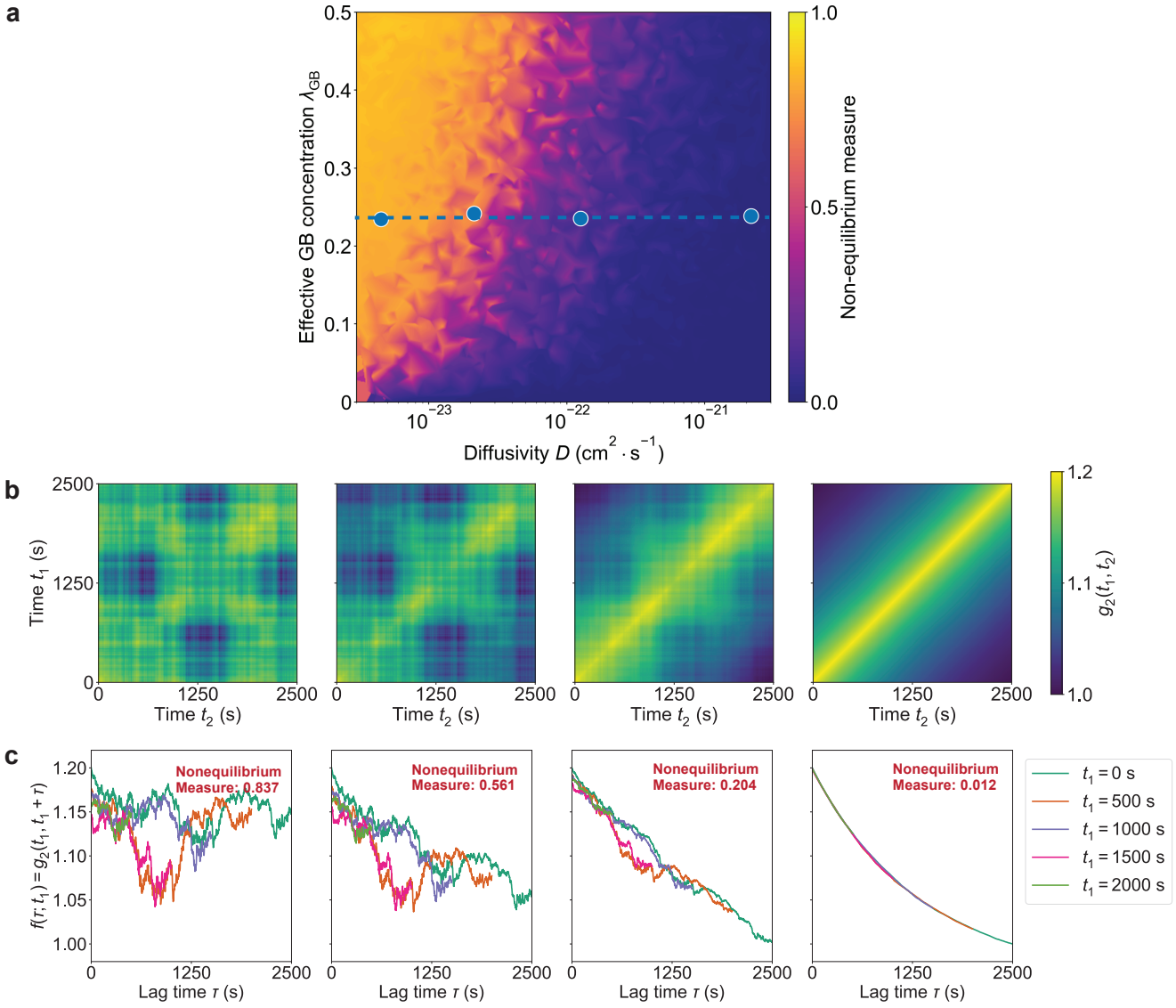


Figure S6. Simulated XPCS dynamics selected along increasing diffusivity at intermediate effective GB concentration. Four simulations near $\lambda_{GB} = 0.24$ show the same diffusivity-driven reduction in $\mathscr{S}_{noneq}$.

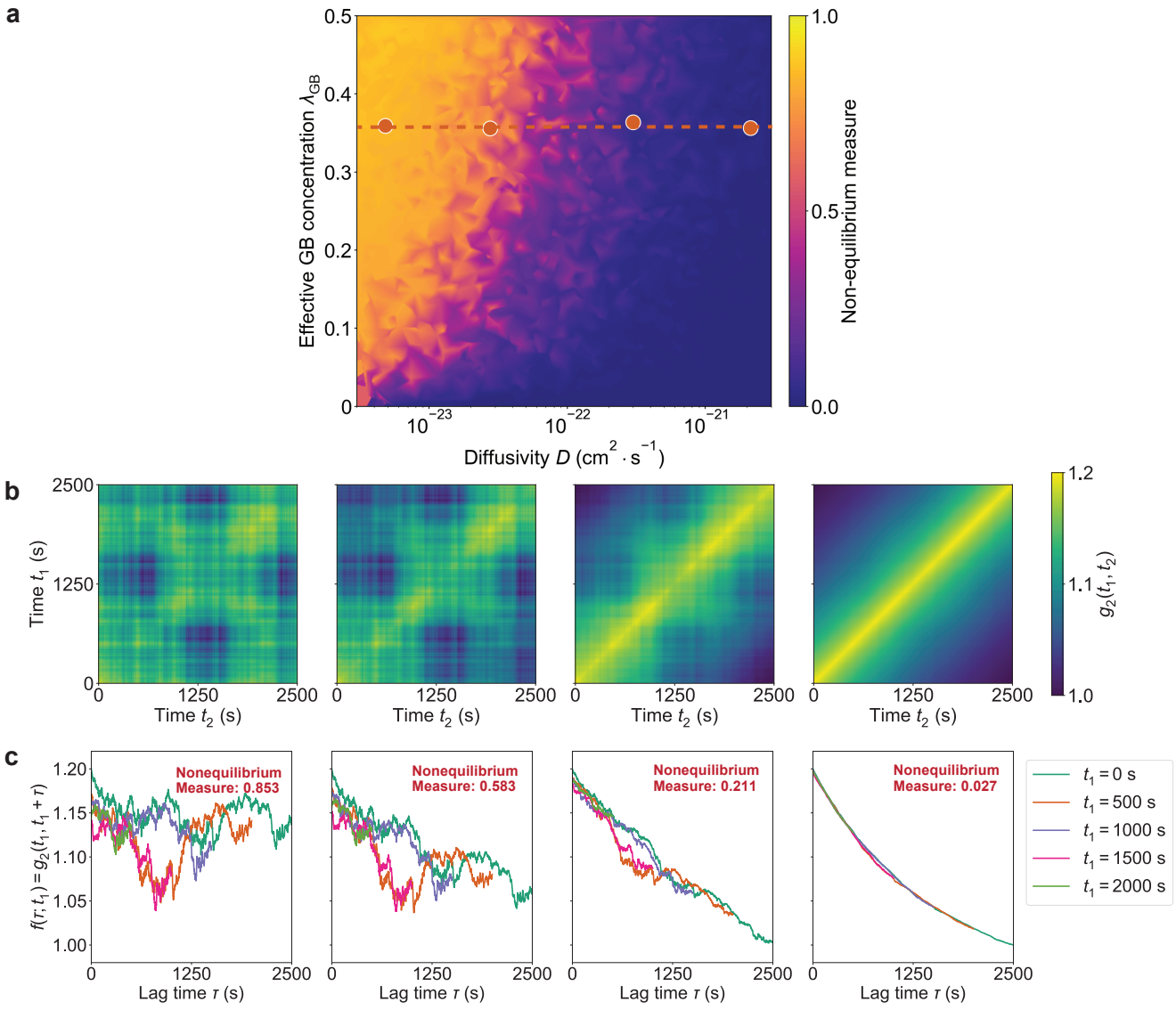


Figure S7. Simulated XPCS dynamics selected along increasing diffusivity at high effective GB concentration. Four simulations near $\lambda_{GB} = 0.36$ demonstrate that a larger GB-associated signal fraction can preserve non-equilibrium signatures to higher diffusivity than in the lower-λ_{GB} slices.

At the low-λ_{GB} slice near $\lambda_{GB} = 0.12$, the selected sequence moves from $D = 3.3 \times 10^{-24}$ to $1.1 \times 10^{-21}\,\mathrm{cm}^2 \cdot \mathrm{s}^{-1}$, while the raw non-equilibrium score falls from $\mathscr{S}_{\mathrm{noneq}} = 0.801$ to 0.010; this indicates that a small GB-associated contribution can still generate a highly non-stationary map when the competing bulk decorrelation is sufficiently slow. At the intermediate slice near $\lambda_{GB} = 0.24$, the corresponding sequence spans $D = 5.9 \times 10^{-24}$ to $9.4 \times 10^{-22}\,\mathrm{cm}^2 \cdot \mathrm{s}^{-1}$ and $\mathscr{S}_{\mathrm{noneq}} = 0.810$ to 0.011. At the higher slice near $\lambda_{GB} = 0.36$, the selected examples follow the same diffusivity trend, with the larger GB-associated signal fraction preserving non-equilibrium signatures to higher diffusivity. These comparisons provide a more quantitative picture of the competition between D and λ_{GB} on the GB dynamics, in which D controls relaxation toward time-translation invariance, and λ_{GB} controls how strongly the slow GB contribution appears in the coherent signal.

2.3 Diffusion from molecular dynamics simulation

To complement the continuum description, we performed classical molecular-dynamics (MD) simulations of a finite $\Sigma5(210)[001]$ Si bicrystal using the EDIP potential on the atomic scale[2]. The simulated cylinder has free lateral surfaces and a periodic axial direction, z, which lies parallel to the GB plane. We therefore use the axial mean-squared displacement (MSD), $\langle \Delta z^2(t) \rangle$, to compare the mobility of atoms initially located near the GB with that of an initial interior reference population. Fig. S8 summarizes the temperature-dependent axial MSD from 300 to 1100 K. At 300-700 K, both populations remain in a bounded, sub-angstrom displacement regime over the 10 ns observation window, and no long-time diffusion coefficient can be reliably inferred. At 900 K, the GB-proximal population develops a clearly larger axial MSD, whereas the interior population remains localized. At 1100 K, both populations exhibit substantial multi-angstrom motion, while the GB-proximal atoms retain the larger axial MSD. These simulations provide an atomistic consistency check for the two-component description in the continuum model, and support treating GB-associated motion as a separate contribution to the scattering dynamics.

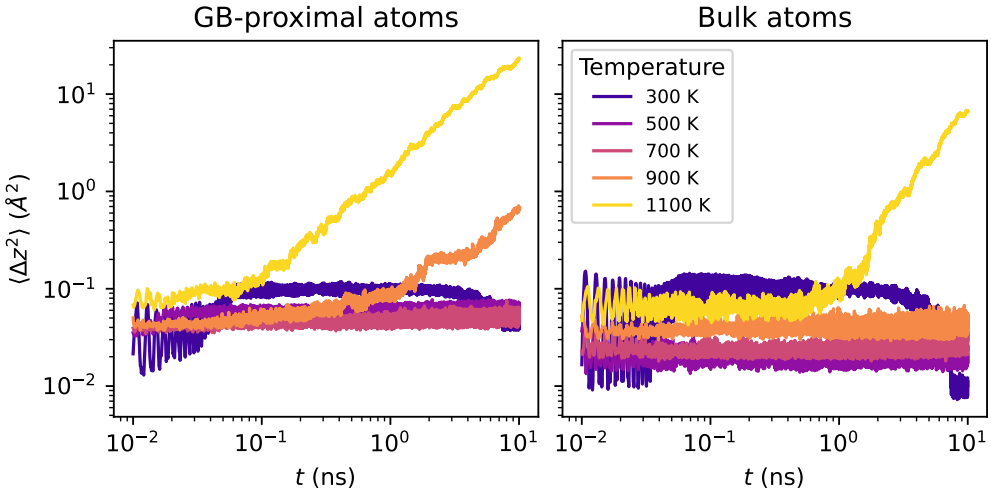


Figure S8. Temperature-dependent axial mean-squared displacement (MSD) from MD simulations of the finite $\Sigma5(210)[001]$ Si bicrystal. The periodic z direction lies parallel to the grain-boundary (GB) plane. Axial mean-square displacement, $\langle \Delta z^2 \rangle$, is shown versus time at 300, 500, 700, 900 and 1100 K for atoms initially proximal to the GB and other interior atoms, classified as bulk.

3 Additional results on domain-adaptive machine learning

In this section, we provide additional details and discussion on the domain-adaptive machine-learning (ML) framework used to extract GB parameters. We also show that domain adaptation is necessary beyond mere experimental data augmentation. Finally, we discuss several failure cases of the current model, in which some experimental data remain outliers outside the learned simulation-to-experiment representation.

3.1 Effects of smearing and rescaling on experimental XPCS data

Before applying domain-adaptive ML, we first test whether the experimental-simulation gap can be bridged by simple transformations of the XPCS maps themselves. In the *smearing* control, each XPCS map is mixed with a locally averaged counterpart computed using a $\sim 50\,\mathrm{s} \times 50\,\mathrm{s}$ temporal averaging window, with mixing weight $\alpha = 0.35$. This control tests whether emulated finite instrumental broadening effects could account for the mismatch. In the *rescaling* control, the off-diagonal values of each map are globally rescaled to the common range $[1.0, 1.2]$, matching the range of experimental data. This ablation study tests the hypothesis that a directly trained regressor fails mainly because of amplitude-scale differences in the maps. In both cases, we train a vanilla convolutional neural network (CNN) purely on the transformed simulated data and then apply the same deterministic transform to the experimental maps before inference.

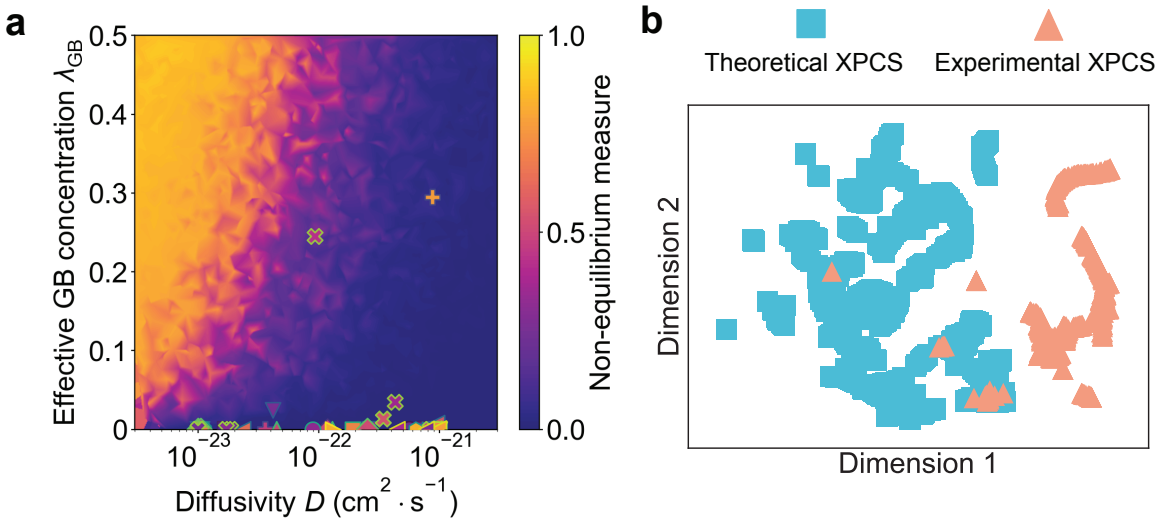


Figure S9. Smearing test on XPCS data without domain adaptation. a. Experimental XPCS spectra inferred by a vanilla CNN trained on smeared simulations and overlaid on the simulated (D, λ_{GB}) non-equilibrium manifold, where the background color denotes the simulated non-equilibrium measure and the experimental marker color denotes the measured $\mathscr{S}_{\mathrm{noneq}}$. **b.** UMAP projection of the corresponding theoretical and experimental XPCS representations, with theoretical spectra shown as blue squares and experimental spectra shown as orange triangles.

The effects of smearing and rescaling are shown in Fig. S9 and Fig. S10, respectively. As shown in Fig. S9, the smearing-control model retains high accuracy on the supervised simulation task, achieving testing set $R^2 = 0.996$ for D and $R^2 = 0.906$ for λ_{GB}. However, the inferred experimental GB parameters still appear out of distribution. Specifically, Fig. S9a shows that 64 out of 68 experimental spectra are assigned to $\lambda_{GB} \leq 0.02$, a regime in which the simulated maps are nearly time-translation invariant over much of the displayed diffusivity range. This assignment is inconsistent with the broad experimental $\mathscr{S}_{\mathrm{noneq}}$ range, which spans from 0.083 to 0.879. The UMAP projection in Fig. S9b is consistent with this interpretation, since the smoothing transform leaves the experimental spectra largely separated from the simulated manifold in the learned representation.

The rescaling control also gives an accurate supervised mapping on transformed simulations, with held-out simulation $R^2 = 0.994$ for D and $R^2 = 0.898$ for λ_{GB}, while failing differently on the experimental spectra. As shown in Fig. S10, the rescaled model assigns 57 of 68 experimental spectra to $\lambda_{GB} \geq 0.25$, while many of these points lie in regions of the simulated phase diagram whose background non-equilibrium measure is much lower than the measured experimental $\mathscr{S}_{\mathrm{noneq}}$ indicated by the marker color. This shift moves experimental spectra away from the lower boundary of the parameter space and leaves them at physically inconsistent locations of the simulated manifold. The failed assignment of GB parameters in Figs. S9, S10a and the separated representation between experiment and simulation in Figs. S9, S10b show that smooth broadening and amplitude rescaling are insufficient for bridging the gap, which motivates a domain-adaptive ML framework with representation-level alignment loss in

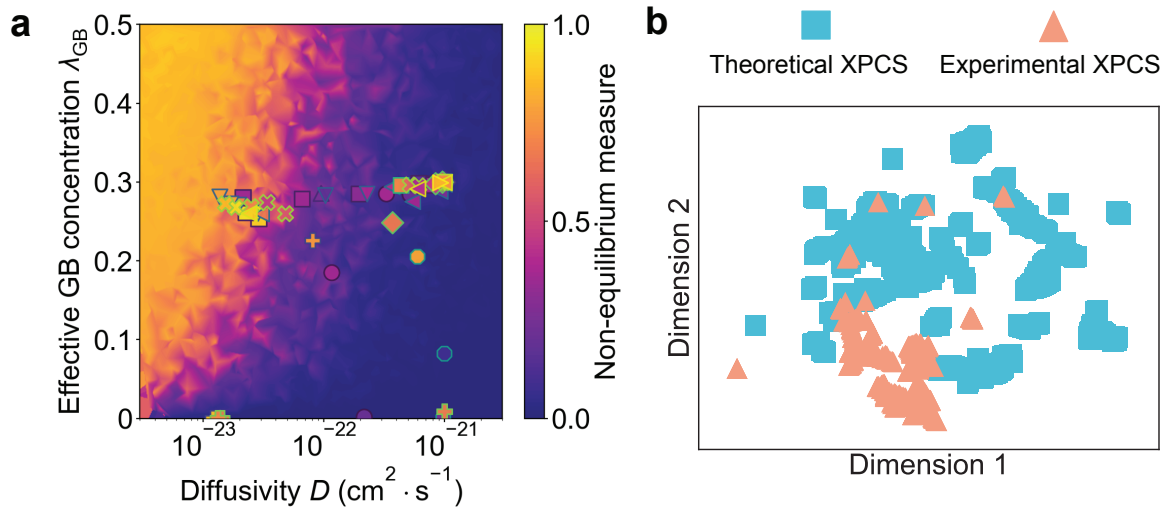


Figure S10. Rescaling test on XPCS data without domain adaptation. a. Experimental XPCS spectra inferred by a vanilla CNN trained on rescaled XPCS data and overlaid on the simulated (D, λ_{GB}) non-equilibrium manifold, where the background color denotes the simulated non-equilibrium measure and the experimental marker color denotes the measured $\mathscr{S}_{noneq}$. **b.** UMAP projection of the corresponding theoretical and experimental XPCS representations, with theoretical spectra shown as blue squares and experimental spectra shown as orange triangles.

the main text.

3.2 Alternative machine-learning methods for domain alignment

In this section, we examine two common alternatives for domain alignment: contrastive learning and min-max adversarial learning. The contrastive model uses the measured $\mathscr{S}_{noneq}$ values to organize embeddings by dynamical similarity, whereas the min-max adversarial model promotes domain-invariant features: the domain classifier is trained to distinguish simulated from experimental spectra, while the feature extractor is trained to make this distinction difficult.

We first show results for contrastive alignment using the InfoNCE-style loss in Fig. S11. The InfoNCE-style uses a contrastive loss for domain adaptation[3], where XPCS maps with similar $\mathscr{S}_{noneq}$ values are encouraged to have nearby embeddings while maps with dissimilar $\mathscr{S}_{noneq}$ values are separated through a soft target distribution. This construction uses the scalar non-equilibrium score as a feature-space organizing variable and leaves the consistency between inferred (D, λ_{GB}) coordinates and the simulated phase manifold to the supervised simulation loss. As shown in Fig. S11a, the model retains moderate simulation-test performance, with $R^2 = 0.847$ for D and $R^2 = 0.880$ for λ_{GB}, but the experimental overlay in Fig. S11b remains strongly biased toward the lower λ_{GB} boundary, with 41 of 68 experimental spectra assigned as $\lambda_{GB} \leq 0.02$. While the UMAP projection in Fig. S11c shows partial overlap between simulated and experimental spectra, the contrastive learning by non-equilibrium similarity appears insufficient to make the predicted physical parameters respect the non-equilibrium structure of the simulated manifold.

Then we perform the adversarial ablation, following the min-max strategy used in adversarial domain-transfer approaches[4,5]. This objective can make the two domains harder to distinguish in feature space, as reflected by the stronger visual mixing in Fig. S12c. At the same time, the parameter regression in Fig. S12a,b suggests that feature-space domain confusion alone is an insufficient criterion for physical inference. Specifically, although the adversarial model preserves the diffusivity regression on simulated data with $R^2 = 0.962$, it largely loses quantitative sensitivity to the GB-associated coordinate, achieving only $R^2 = 0.039$ for λ_{GB}. The predicted λ_{GB} values collapse into a narrow band around $\lambda_{GB} \simeq 0.14$, indicating that the model no longer resolves λ_{GB} variations even on labeled simulations. As a result, the extracted GB parameters for experimental data in Fig. S12b concentrate near $\lambda_{GB} \simeq 0.14$

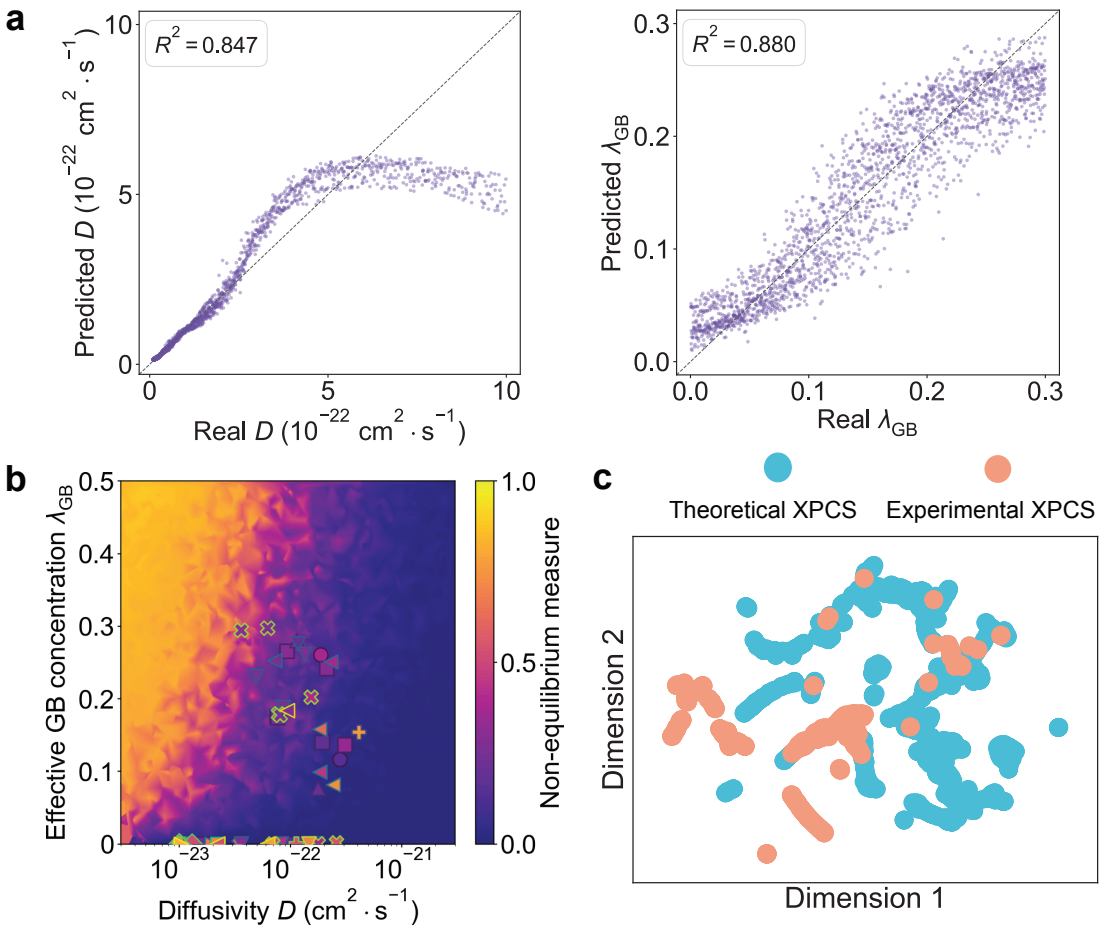


Figure S11. InfoNCE-style contrastive alignment for experiment-simulation domain transfer. a. Predicted and true simulation parameters for the InfoNCE-trained model, with separate test-set regressions for D and λ_{GB}. **b.** Experimental spectra inferred by the same model and overlaid on the simulated (D, λ_{GB}) non-equilibrium manifold; the background color denotes the simulated non-equilibrium measure, and the color of each experimental marker denotes the measured experimental $\mathscr{S}_{noneq}$. **c.** UMAP projection of the theoretical and experimental XPCS representations learned with the InfoNCE-style objective.

rather than near $\lambda_{GB} \simeq 0$. This should therefore be interpreted as a regression collapse caused by the adversarial objective.

Compared to these methods, our approach, which combines the CORAL alignment[6] with the non-equilibrium consistency constraint, achieves a more stable balance between supervised parameter regression on simulated data and domain alignment between simulation and experiment. This is likely because our combination penalizes a domain mismatch in the representation while also retaining a physical constraint on where experimental spectra can be placed in the simulated (D, λ_{GB}) manifold.

3.3 Ablation tests on hyperparameters

The total training loss in our domain-adaptive ML framework, as shown in the main text, is given by $\mathscr{L} = \mathscr{L}_y + w_{CORAL}\mathscr{L}_{CORAL} + w_{sur}\mathscr{L}_{sur}$. Here, the domain loss $\mathscr{L}_d = w_{CORAL}\mathscr{L}_{CORAL} + w_{sur}\mathscr{L}_{sur}$ contains two terms scaled by hyperparameters w_{CORAL} and w_{sur}. The CORAL weight w_{CORAL} sets the strength of feature-statistic alignment between simulated and experimental XPCS maps, and the surrogate weight w_{sur} sets the strength of the experimental non-equilibrium consistency constraint imposed through the relation between inferred parameters and

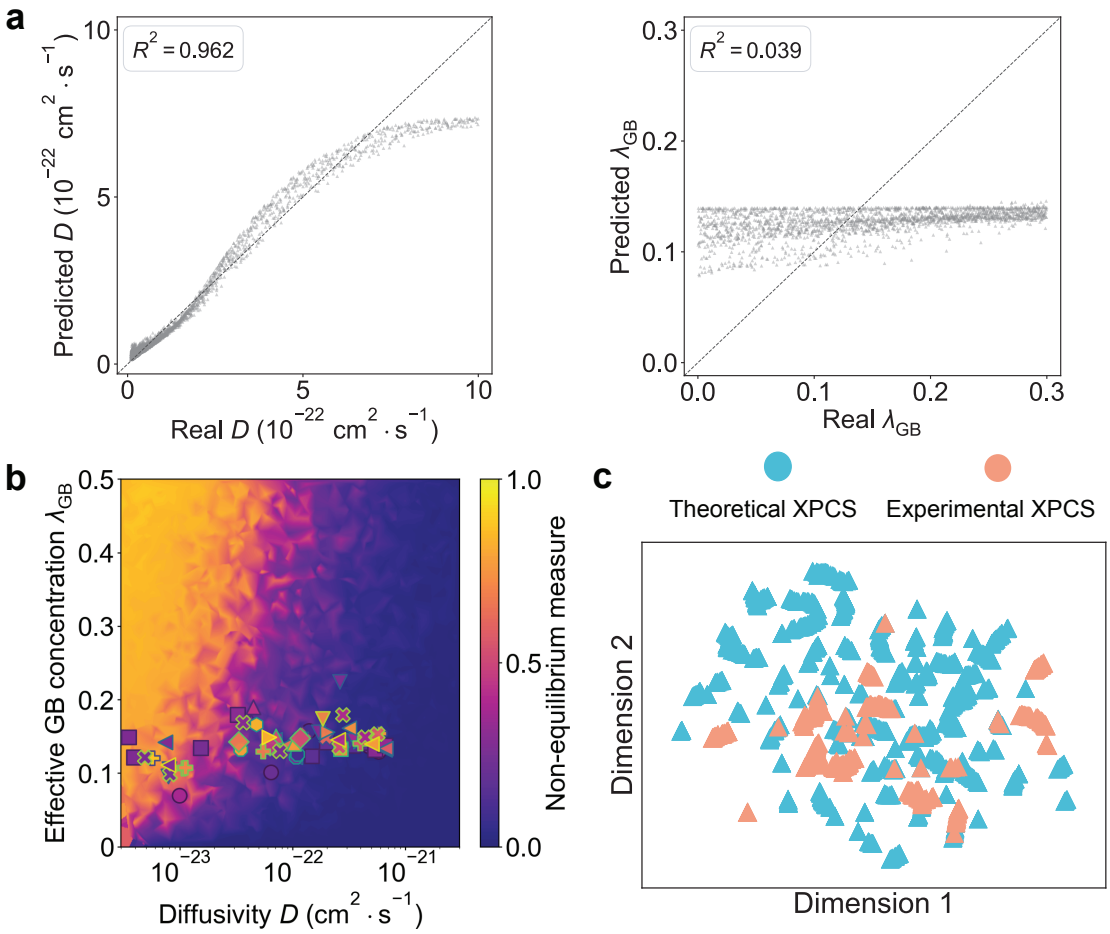


Figure S12. Min-max adversarial alignment for experiment-simulation domain transfer. a. Predicted and true simulation parameters for the adversarially aligned model, showing accurate simulation-test regression for D and a nearly collapsed prediction of λ_{GB}. **b.** Experimental spectra inferred by the adversarial model and overlaid on the simulated $(D, \lambda_{\mathrm{GB}})$ non-equilibrium manifold; the background color denotes the simulated non-equilibrium measure, and the color of each experimental marker denotes the measured experimental $\mathscr{S}_{\mathrm{noneq}}$. **c.** UMAP projection of the theoretical and experimental XPCS representations learned with the min-max domain-confusion objective.

$\mathscr{S}_{\mathrm{noneq}}$. In this section, we vary the two weights in our domain loss to check whether the chosen setting remains stable across nearby choices.

The results are tabulated in Table S1, where we report the held-out simulation R^2 for the two physical parameters together with the mean absolute error between the measured experimental $\mathscr{S}_{\mathrm{noneq}}$ and the surrogate-predicted $\mathscr{S}_{\mathrm{noneq}}$ from the inferred parameters.

w_{CORAL}	w_{sur}	R^2_D	$R^2_{\lambda_{\mathrm{GB}}}$	Experimental $\mathscr{S}_{\mathrm{noneq}}$ MAE
1.00	0.0	0.964	0.863	0.204
1.00	0.3	0.944	0.876	0.105
1.00	0.6	0.948	0.881	0.082
1.00	**1.2**	**0.943**	**0.877**	**0.074**
1.00	2.0	0.920	0.882	0.066
2.00	1.2	0.889	0.860	0.072
4.00	1.2	0.837	0.805	0.081

Table S1. Sensitivity of the CORAL and non-equilibrium-surrogate loss weights. All models are trained under the same simulation and experimental data configuration while varying w_{CORAL} and w_{sur} in the domain-adaptation objective. The bold row denotes the weight setting used in our final method.

With $w_{\mathrm{sur}} = 1.2$ fixed, increasing w_{CORAL} from 1 to 4 reduces the simulation R^2, with the diffusivity R^2 falling to 0.889 at $w_{\mathrm{CORAL}} = 2$ and to 0.837 at $w_{\mathrm{CORAL}} = 4$, accompanied by a comparable degradation in the λ_{GB} regression. This trend indicates that the feature-alignment term should remain bounded, because excessive domain matching erodes the simulation-derived parameter structure that the inference is meant to preserve.

With $w_{\mathrm{CORAL}} = 1$ fixed, setting $w_{\mathrm{sur}} = 0$ leaves the experimental non-equilibrium consistency poor, with an experimental $\mathscr{S}_{\mathrm{noneq}}$ MAE of 0.204 despite accurate simulation regression. Increasing w_{sur} reduces this inconsistency substantially, while very large surrogate weight begins to trade away diffusivity accuracy. Our final setting, $w_{\mathrm{CORAL}} = 1.0$ and $w_{\mathrm{sur}} = 1.2$, therefore represents a balanced option that keeps both simulation regressions in the same accuracy range as neighboring weight choices, imposes a stronger experimental non-equilibrium constraint than the feature loss alone, and avoids the sharper simulation-regression degradation seen at larger CORAL weights.

3.4 Outlier experimental XPCS data on the simulated parameter manifold

After CORAL alignment, non-equilibrium surrogate regularization, and material-wise fine-tuning, most experimental maps move into the crossover region of the simulated $(D, \lambda_{\mathrm{GB}})$ manifold. Fig. S13 focuses on the small group that remains assigned to the lower edge of the λ_{GB} coordinate.

The 8 boundary-assigned spectra all lie at the lower edge of the inferred parameter range, with median $D = 1.0 \times 10^{-23}\,\mathrm{cm}^2 \cdot \mathrm{s}^{-1}$, median $\Gamma = 2.0 \times 10^{18}\,\mathrm{s} \cdot \mathrm{cm}^{-2}$, and λ_{GB} numerically at zero or near zero, while the remaining 60 experimental spectra have a median $\lambda_{\mathrm{GB}} = 0.0356$ and a much larger fraction lying inside the sampled simulation bounds. The measured non-equilibrium scores of the boundary-assigned group span a wide range from $\mathscr{S}_{\mathrm{noneq}} = 0.084$ to 0.882 with a mean of 0.596, inconsistent with their common assignment near $\lambda_{\mathrm{GB}} = 0$ by the ML model. This point is visible in the zoomed phase diagram in Fig. S13, where several experimental markers near the lower boundary have bright marker colors even though the local simulated background in the same low-λ_{GB} region corresponds to a much lower non-equilibrium measure.

The representative maps in Fig. S13 show that the low-λ_{GB} assignments include several distinct forms of GB dynamics, rather than a single experimental morphology. For example, map A exhibits a comparatively continuous decorrelation ridge whose width and curvature evolve across the measurement window, map B shows a sharp temporal separation between two correlation regimes, while map C displays a highly heterogeneous two-time texture with pronounced horizontal and vertical banding. When such spectra are projected onto the learned simulation landscape, the inference necessarily returns the nearest available simulated regime, which in these cases lies along the low-λ_{GB} edge. These cases suggest a current limitation of our framework, namely that our current integrated

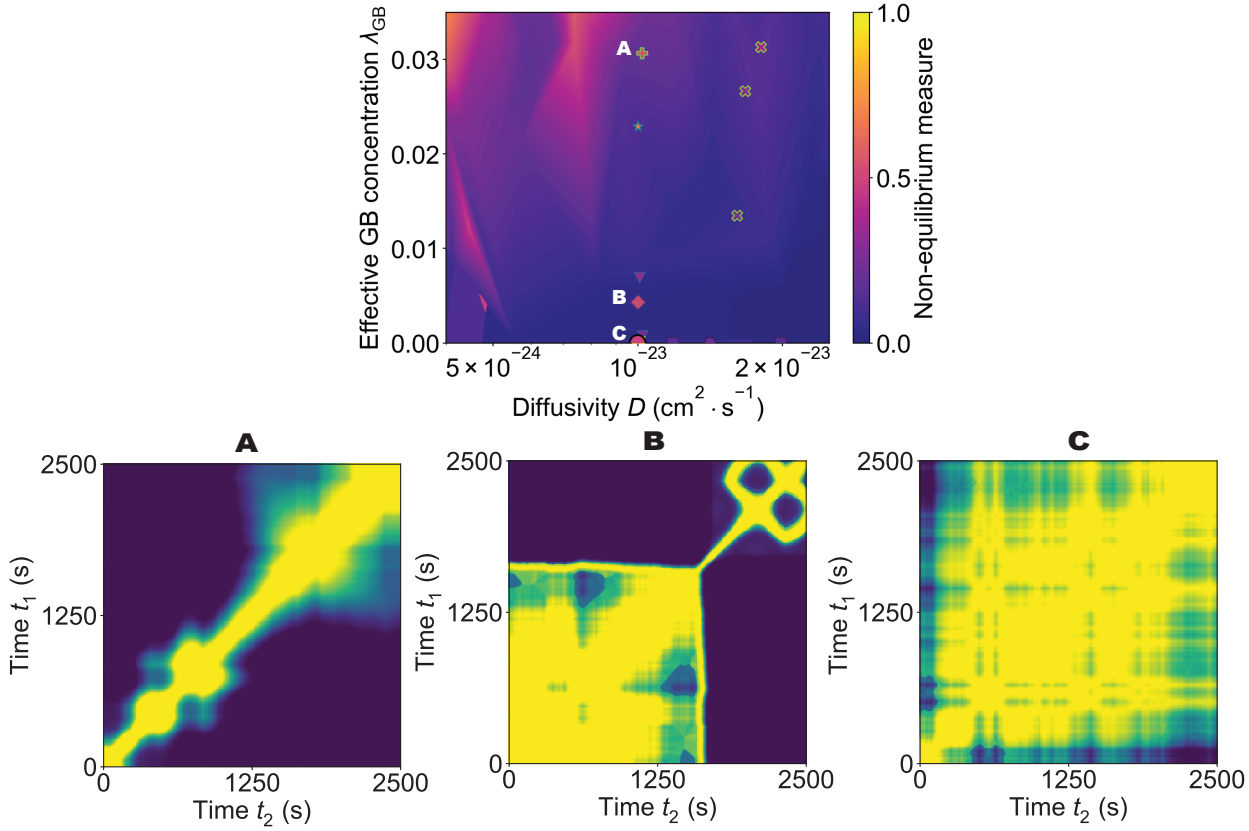


Figure S13. Boundary-assigned experimental XPCS near the low-λ_{GB} edge of the inferred phase manifold. The top panel shows a zoomed view of the simulated non-equilibrium phase map at small λ_{GB}, with experimental spectra overlaid using marker colors that denote their measured experimental $\mathscr{S}_{\text{noneq}}$. The labelled points identify representative experimental maps shown below, where A, B, and C illustrate distinct two-time correlation structures assigned to the same low-λ_{GB} region.

ML-theory-experiment framework does not yet span all experimentally observed forms of non-stationary GB dynamics. Improving this coverage will likely require more representative experimental data and a more flexible simulation model that incorporates additional mechanisms in GB dynamics.

References

1. Leheny, R. L. Xpcs: Nanoscale motion and rheology. *Curr. opinion colloid & interface science* **17**, 3–12 (2012).
2. Justo, J. F., Bazant, M. Z., Kaxiras, E., Bulatov, V. V. & Yip, S. Interatomic potential for silicon defects and disordered phases. *Phys. review B* **58**, 2539 (1998).
3. Oord, A. v. d., Li, Y. & Vinyals, O. Representation learning with contrastive predictive coding. *arXiv preprint arXiv:1807.03748* (2018).
4. Chen, X. *et al.* Detecting thermodynamic phase transition via explainable machine learning of photoemission spectroscopy. *Newton* **1** (2025).
5. Nelson, K., Kreiman, T., Levine, S. & Krishnapriyan, A. S. Bridging the simulation-to-experiment gap with generative models using adversarial distribution alignment. *arXiv preprint arXiv:2604.01169* (2026).
6. Sun, B. & Saenko, K. Deep coral: Correlation alignment for deep domain adaptation. In *European conference on computer vision*, 443–450 (Springer, 2016).